RSC Advances

PAPER

Cite this: *RSC Adv.*, 2023, **13**, 8163

Towards hard-magnetic behavior of $CoFe_2O_4$ nanoparticles: a detailed study of crystalline and electronic structures, and magnetic properties

D. H. Manh, *[a] T. D. Thanh,[a] T. L. Phan[bc] and D. S. Yang[d]

Received 25th January 2023
Accepted 5th March 2023

DOI: 10.1039/d3ra00525a

rsc.li/rsc-advances

We have used the coprecipitation and mechanical-milling methods to fabricate $CoFe_2O_4$ nanoparticles with an average crystallite size (d) varying from 81 to ~12 nm when changing the milling time (t_m) up to 180 min. X-ray diffraction and Raman-scattering studies have proved the samples crystalizing in the spinel structure. Both the lattice constant and residual strain tend to increase when $t_m(d)$ increases (decreases). The analysis of magnetization data has revealed a change in the coercivity (H_c) towards the hard-magnetic properties. Specifically, the maximum H_c is about 2.2 kOe when $t_m = 10$ min corresponding to $d \approx 29$ nm; beyond this $t_m(d)$ value, H_c gradually decreases. Meanwhile, the increase of t_m always reduces the saturation magnetization (M_s) from ~69 emu g^{-1} for $t_m = 0$ to 35 emu g^{-1} for $t_m = 180$ min. The results collected as analyzing X-ray absorption data have indicated a mixed valence state of $Fe^{2+,3+}$ and Co^{2+} ions. We think that the migration and redistribution of these cations between the tetrahedral and octahedral sites together with lattice distortions and defects induced by the milling process have impacted the magnetic properties of the $CoFe_2O_4$ nanoparticles.

1 Introduction

Spinel-type ferrite oxides are important materials used widely in many technological applications, including permanent magnets, high-density data storage, rechargeable lithium-ion batteries, microwave absorbers, electromagnetic generators, aqueous supercapacitors, and biomedical labeling.[1–5] Their chemical formula is generalized as AB_2O_4, where A and B are usually divalent and trivalent cations, respectively. They crystallize in a cubic lattice, and belong to the $Fd\bar{3}m$ space group. Their unit cell consists of eight formula units, with two types of interstitials: (i) tetrahedral interstitials are surrounded by four oxygen atoms (called A sites), and (ii) octahedral ones are surrounded by six oxygen atoms (B sites). A and B metal cations can reside in eight tetrahedral sites and 16 octahedral sites, respectively. We would obtain a normal or inverse spinel type depending on the residence ratio of A and B in these sites. The structure is called a normal spinel if the A cations completely occupy the tetrahedral sites and the B cations completely occupy the octahedral sites. In contrast, if the tetrahedral sites are occupied half by the A cations, and the octahedral sites are occupied by all the B cations and half of the A cations, the structure is called an inverse spinel.[1,3] However, when modifying synthesis conditions and the crystal size, a random distribution of A and B at the tetrahedral and octahedral sites would happen, leading to the so-called mixed spinel type. Its chemical formula is thus defined as $(A_\delta^{2+}B_{1-\delta}^{3+})[A_{1-\delta}^{2+}B_{1+\delta}^{3+}]O_4^{2-}$, where δ is the degree of inversion, and the round and square brackets are indicative of the A (tetrahedral) and B (tetrahedral) sites, respectively. This formula can be generalized for all spinel types: a normal spinel with $\delta = 1$, an inverse spinel with $\delta = 0$, and a mixed spinel with $0 < \delta < 1$.[6] Apart from the changes related to the particle size and the valence of the cations (because A and B ions can have different oxidation states), the change in value of δ (the cation distribution) also influences strongly the optical, electrical and magnetic properties of spinel ferrites.

So far, many intriguing electrical and magnetic properties in spinel ferrites have been discovered, such as (A, B)-sublattice-related exchange interactions, orbital-/charge-ordering, metal-insulator transition, magnetic frustration, spin-lattice coupling, and Verwey transition,[3,7] which could be controlled by the substitutions at that A and B sites. These properties together with technological application potentials have attracted intensive interest of the solid-state-physics community, specially nanostructured spinel ferrites that have more unique characters different from bulk counterparts.[1,8–11] It has been believed that a surface-area-to-volume ratio of nanostructures is large, and additionally provides the structural degrees of freedom. Among nanostructured spinel ferrites, cobalt spinel ferrite ($CoFe_2O_4$) has attracted much more research interest

[a]Institute of Materials Science, Vietnam Academy of Science and Technology, 18 Hoang Quoc Viet, Hanoi, Viet Nam. E-mail: manhdh.ims@gmail.com
[b]Department of Physics, Hankuk University of Foreign Studies, Yongin 449-791, South Korea
[c]Faculty of Engineering Physics and Nanotechnology, VNU-University of Engineering and Technology, 144 Xuan Thuy, Cau Giay, Ha Noi, Viet Nam
[d]Department of Science Education, Chungbuk National University, Cheongju 360-763, South Korea

since it has outstanding magnetic, magneto-elastic/optical, magnetophototronic, and photo-magnetic properties.[12–14] Most markedly, it is classified as a semi-hard material with a large magneto-crystalline anisotropy and saturation magnetization that can used to fabricate rare-earth-free permanent magnets.[15–17] Similar to $NiFe_2O_4$, $CoFe_2O_4$ is well known as an inverse spinel (notably, $ZnFe_2O_4$ is a normal spinel while $(Mg,Zn)Fe_2O_4$ is a mixed spinel),[18] in which the Co^{2+} cations occupy the B sites while the Fe^{3+} cations occupy both the A and B sites, meaning $(Fe^{3+})[Co^{2+}Fe^{3+}]O_4$.[19,20] Having modified fabrication conditions and the crystal size, the proportion of Co^{2+} and Fe^{3+} in the A and B sites would be changed, consequently the degree of inversion δ. Together with δ, surficial defects and lattice distortions also strongly influence the magnetic properties of $CoFe_2O_4$, which are characterized by the magnitudes of the coercivity (H_c), saturation magnetization (M_s), and remanent magnetization (M_r).

It has been used various techniques to synthesize nanostructured $CoFe_2O_4$ materials, such as magnetron sputtering,[21] hydrothermal method,[11,22,23] sol–gel method,[23] and combustion, coprecipitation and precipitation methods.[24] Depending on synthesis methods and conditions, the values of H_c, M_r, and M_s would be different. Among these parameters, H_c is considered as a key parameter characteristic of the magnetic hardness of cobalt ferrite, which is ascribed to the occupation of Co^{2+} because it is ascribed to be a highly anisotropic ion.[25,26] In practice, it can be tuned H_c *via* fabricating core/shell nanomaterials,[27] nanocomposites,[17,28] and nanostructures (nanoparticles, nanowires, nanofibers, nanoribbons, and thin films).[21,23,24,29,30] It is clear that an enhancement in H_c can be realized upon changing the crystal shape and particle size, and/or creating a high level of residual lattice strain and distortions inside particles. Because of these features, some research groups prepared $CoFe_2O_4$ by using hydrothermal, coprecipitation and sol–gel methods, and then carried out high-energy ball milling to produce $CoFe_2O_4$ nanoparticles (NPs) with different sizes and different levels of lattice strain and distortions upon controlling the milling time (t_m), consequently high magnetic performance.[13,16,31–33] In those studies, the researchers employed X-ray/electron diffraction and/or Mössbauer spectroscopy to figure out the relations between the particle size, microstructures and cation distribution, and the magnetic properties, without directly using sensitive tools in order to identify Co and Fe oxidation states. To get more knowledge about $CoFe_2O_4$ NPs prepared by the mechanical ball milling method, we shall use X-ray diffraction accompanied with Rietveld refinement, Raman spectroscopy, and X-ray absorption spectroscopy to analyze the structural characterization, and electronic structure *versus* the milling process (t_m), and then evaluate carefully their impacts on the magnetic properties.

2 Experimental details

First, a large amount of $CoFe_2O_4$ in powder was synthesized by a conventional coprecipitation method. Initial chemicals including $CoCl_2\cdot6H_2O$ and $FeCl_2\cdot4H_2O$ (98%) ordered from Sigma-Aldrich were used as precursors. To produce Co^{2+} and Fe^{2+} containing solutions, we dissolved 4 mmol $CoCl_2\cdot6H_2O$ and 8 mmol $FeCl_2\cdot4H_2O$ in 70 ml and 30 mL distilled water, respectively. After that, the Fe^{2+} solution was dropped into the Co^{2+} solution. The pH of the mixture was adjusted by controlling NH_4OH amount. The mixture was firstly stirred at room temperature for 30 min, and then transferred to Teflon-line autoclaves. The autoclaves were tightly sealed, heated to 180 °C and kept at this temperature for 24 h. After completing chemical reactions, precipitation was collected upon centrifuging at 8000 rpm, and washed several times to remove excess precursors. The collected powder sample was treated at 200 °C for 3 h to evaporate water. After dried, it was divided into small parts of ~0.3 g. These parts were in turn taken to mill in normal atmosphere for different milling times (t_m) ranging from 1 to 180 min (hereafter, the as-prepared sample is labelled as $t_m = 0$), see Table 1 for more details. The milling process was carried out in air using a SPEX SamplePrep Mixer/Mill, and the set of stainless-steel grinding media (vial and balls).

After milled, the final products were checked the particle morphology by a field emission scanning electron microscope (SEM, JSM-5410LV) that was linked with X-ray energy dispersive spectroscopy (EDS). Their crystal structure was characterized by a Bruker X-ray diffractometer equipped with the copper K_α radiation. The Rietveld refinement method was also used to analyze X-ray diffraction (XRD) patterns, allowing us to evaluate the structural parameters, crystallite size, and lattice strain. In addition to XRD, an XploRA PLUS Raman spectrometer (Horiba) was used to judge structure phases, in which a laser wavelength of 785 nm was used as an excitation source. To identify the oxidation state of the cations in $CoFe_2O_4$, we utilized X-ray absorption spectroscopy (XAS). XAS measurements on the powder samples were carried out under the transmission configuration. The magnetic properties were investigated through magnetic-field-dependent magnetization, $M(H)$, measurements, which were performed on a conventional vibrating sample magnetometer.

3 Results and discussion

We have selected typical samples to check their particle size and surface morphology by means of an electron microscope.

Table 1 Some experimental values obtained as analyzing XRD patterns and $M(H)$ data of mechanically-milled $CoFe_2O_4$ NPs

t_m (min)	d (nm)	ε	B × 10^{-6} (Oe^2)	H_a (kOe)	$K_1 \times 10^{-6}$ (erg g^{-1})
0	80.9	0.0017	2.52	6.15	0.210
1	80.2	0.0015	2.51	6.13	0.198
2	50.6	0.0027	2.62	6.26	0.200
4	55.7	0.0025	2.47	6.08	0.197
8	40.4	0.0034	2.49	6.12	0.192
10	29.3	0.0047	2.95	6.65	0.200
20	17.9	0.0075	3.69	7.44	0.201
40	12.8	0.0107	3.39	7.13	0.170
60	12.3	0.0111	2.99	6.70	0.139
120	11.6	0.0118	2.90	6.59	0.130
180	12.4	0.0111	2.68	6.34	0.111

Fig. 1(a)–(f) show representative micrographs of the samples with $t_m = 0$, 4, 10, 20, 60, and 180 min, which were recorded with the same scale bar. One can see that particles in the samples have irregular shapes and random orientation. While the particle size of the as-prepared sample ($t_m = 0$) is about 200–400 nm, see Fig. 1(a), that of the other samples is much smaller. It is hard to exactly evaluate the size distribution if basing on the micrographs, particularly for the samples with $t_m > 10$ min, see Fig. 1(d)–(f). For the milled samples, their NPs aggregate to form large clusters. This phenomenon is popular for nanomaterials,[15,34] and assigned to attractive magnetic and/or electrostatic forces existing among NPs.[35,36]

Together with the inspection of the particle morphology, the presence of elements in the samples has also been checked. Fig. 2 shows typical EDS spectra of the samples with $t_m = 0$, 60 and 180 min, which were recorded within an area of $\sim 0.02 \times 0.02$ mm^2, see the inset of Fig. 2. Apart from a weak peak of carbon (C) at ~0.25 keV, some strong peaks at energies $E = 0.4$–8.1 keV are from Co, Fe and O of cobalt ferrites. For the $t_m = 0$ sample, weight (atomic) percentage values of Co, Fe and O averaged from different measurement positions are about 20.3 (9.8), 40.4 (20.6), and 39.3 (69.6)%, respectively. For the samples with $t_m = 60$ and 180 min, the concentration of these elements changed within few percentages. This could be due to oxygen absorbency (from air) at the surface, and grinding-media-related contaminations that happen as decreasing the NP size.

The crystal structure has also been characterized by using an X-ray diffractometer. Diffraction patterns in the angle range of $2\theta = 15$–80° are shown in Fig. 3. The analysis has revealed that the XRD pattern of the as-prepared $CoFe_2O_4$ sample is fully indexed to the spinel cubic structure with the $Fd\bar{3}m$ symmetry and lattice constants $a = b = c \approx 8.4$ Å, consistent with previous studies.[15,16,22,23,25] Furthermore, the Rietveld refinement using a structural model reported for the cubic-spinel phase[37] provided a satisfactory fit to the experimental data (see Fig. 3), confirming a single phase of the $t_m = 0$ sample. As increasing

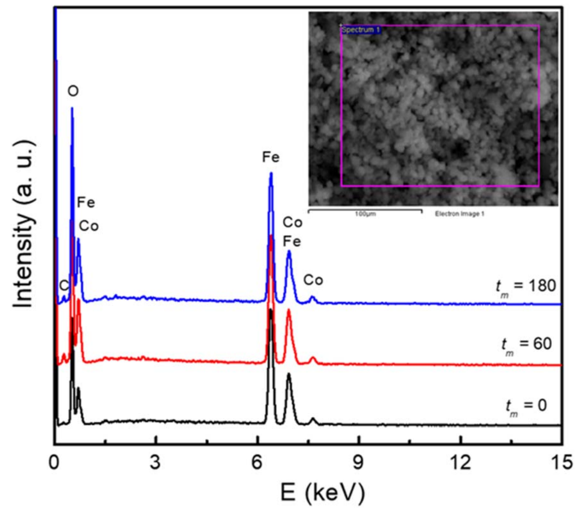

Fig. 2 EDS spectra of typical samples with $t_m = 0$, 60, and 180 min. Inset: a selected area for recording EDS data.

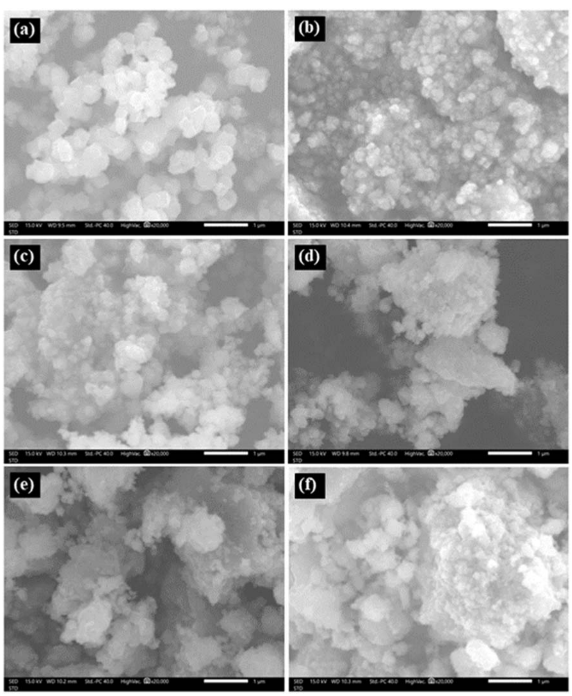

Fig. 1 Micrographs of typical NP samples with $t_m = 0$ (a), 4 (b), 10 (c), 20 (d), 60 (e) and 180 (f) min, which were recorded as fixing scale bars of 1 μm.

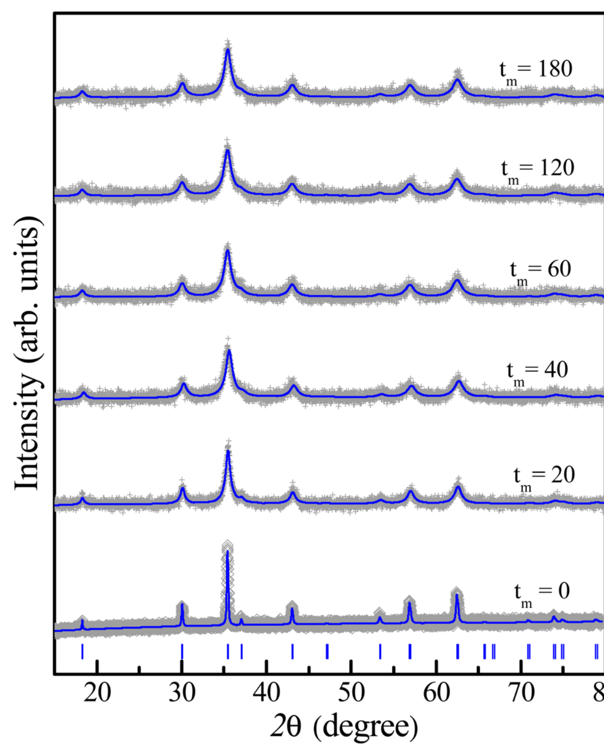

Fig. 3 Rietveld refinement of XRD patterns of some representative samples with different milling times t_m, in which blue vertical bars show standard diffraction lines of the spinel structure.

t_m, the feature of diffraction patterns remains unchanged, except the peak broadening due to a decrease in the crystallite size as discussed below. This proves the stability of the cubic spinel phase of $CoFe_2O_4$ NPs *versus* the mechanical milling.

Based on 2θ-position dependences and the peak broadening value (β) after subtracting instrumental broadening contributions, the crystallite size (d) and lattice strain (micro-deformation, ε) as a function of t_m were estimated upon the Williamson–Hall (WH) theory generalized by the equation of $\beta \cos\theta = (k\lambda/d) + 2\varepsilon \sin\theta$, where $k = 0.9$ is the shape factor.[38] The obtained d and ε data are listed in Table 1 for reference. We have found that d and ε data can be described by t_m-dependent exponential functions of $d(t_m) = 67.74 \times \exp(-0.129 \times t_m) + 12.36$ and $\varepsilon(t_m) = -0.011 \times \exp(0.045 \times t_m) + 0.012$, respectively, see Fig. 4. A rapid decrease (increase) of $d(\varepsilon)$ takes place when t_m changes from 1 to 40 min. As $t_m > 40$ min, d and ε are less changed and approach to the critical values of about 12 nm and 0.011, respectively. Change tendencies of d and ε with respect to t_m are also analogous to those recorded for other $CoFe_2O_4$ NPs fabricated by mechanical milling.[13,31,33] Depending on the size of initial $CoFe_2O_4$ powders, the mass ratio of balls to powders, and t_m value, it could be decreased d to a critical value of $d_c \approx 9$ nm.[31,33]

Another interesting result obtained from the XRD refinement is an anomalous evolution of the lattice parameter (a) as a function of $t_m(d)$ as shown Fig. 5(a) and its inset. In the interval of $t_m = 1$–10 min (d reduces from ~80 to ~29 nm), a slightly increases with increasing t_m. Beyond $t_m = 10$ min ($d \approx 29$ nm), it sharply increases with further increasing t_m (*i.e.*, decreasing d). A similar expansion of the lattice parameters *versus* decreasing the particle size has also been reported on CeO_{2-x} and $BaTiO_3$ NPs, which was attributed to a decreased electrostatic force caused by valence reduction of Ce and an increased ionicity of Ti, respectively.[39] On the other hand, we have also observed an significant change in the intensity ratio of $I_{(220)}/I_{(222)}$ with respect to $t_m(d)$, where $I_{(220)}$ and $I_{(222)}$ are the integrated intensities of (220) and (222) peaks, respectively, see Fig. 5(b) and its inset. This ratio reflects the cation distribution

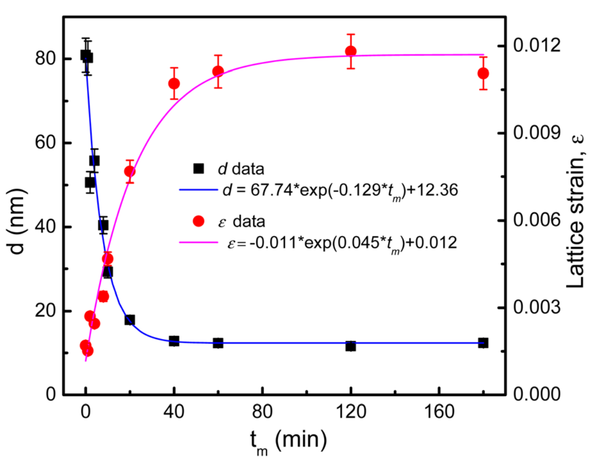

Fig. 4 Variations of d and ε data according to exponential functions of t_m.

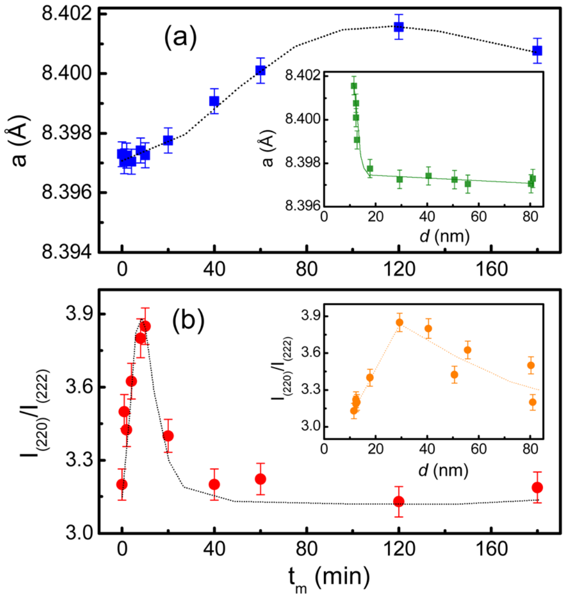

Fig. 5 Variations of (a) the lattice constant, and (b) $I_{(220)}/I_{(222)}$ as a function of t_m. The insets show the variation of these parameters with respect to the crystallite size d.

at the A and B sites in cobalt ferrite.[40] Concretely, it displays a maximum at $t_m = 10$ min ($d \approx 29$ nm), and beyond this $t_m(d)$ value, it gradually decreases. We believe that the cation distribution is a main factor influencing the lattice properties of the milled $CoFe_2O_4$ NPs.

We have also used Raman scattering (RS) spectroscopy to consider how characteristic phonon modes of $CoFe_2O_4$ NPs changes with respect to t_m. This is known as a sensitive and non-destructive tool accompanied with XRD to assess the crystalline structure. According to the group theory's prediction, near the center of Brillouin zone ($q = 0$, the conservation of momentum vector), cobalt ferrite $CoFe_2O_4$ with the $Fd\bar{3}m$ spinel structure (O_h^7 symmetry) has five Raman active modes, $\Gamma = A_{1g} + E_g + 3T_{2g}$, associated with the motion of O and A-/B-site atoms.[41] Energy order of the modes is addressed as follows: $A_{1g}(1) > A_{1g}(2) > T_{2g}(1) > T_{2g}(2) > E_g > T_{2g}(3)$.[42] In the current work, we have observed all of these modes in RS spectra of $CoFe_2O_4$ NPs, see Fig. 6 that plots RS data of some representative samples, normalized to the $T_{2g}(2)$-mode intensity. For the $t_m = 0$ sample, its spectrum consists of the modes peaked at about 193, 303, 475, 566, 617 and 686 cm^{-1} associated to $T_{2g}(3)$, E_g, $T_{2g}(2)$, $T_{2g}(1)$, $A_{1g}(2)$ and $A_{1g}(1)$ symmetries, respectively, as labelled in Fig. 6. Basically, 617 cm^{-1} ($A_{1g}(2)$) and 686 cm^{-1} ($A_{1g}(1)$) are associated with symmetric stretching of O atoms *versus* Co and/or Fe atoms in the tetrahedral (AO_4) sites.[41,43] It should be noticed that as studying Fe_3O_4, at frequencies above 600 cm^{-1}, it is only observed one mode due to A_{1g}.[44,45] The A_{1g}-band splitting into two sub-bands $A_{1g}(1)$ and $A_{1g}(2)$ in $CoFe_2O_4$ hints that 686 cm^{-1} ($A_{1g}(1)$) and 617 cm^{-1} ($A_{1g}(2)$) are related to FeO_4 and CoO_4 tetrahedra, respectively.[41,46] One can thus rely upon their intensity ratio ($A_{1g}(1)/A_{1g}(2)$) to assess the cation distribution at the A and B sites. Meanwhile, the other modes

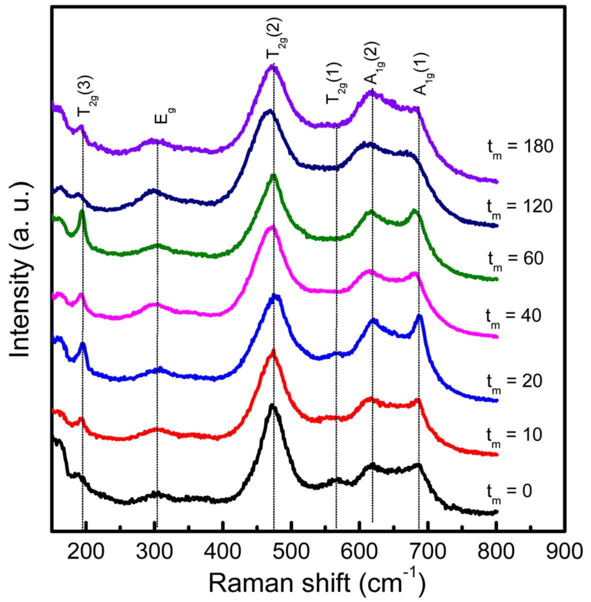

Fig. 6 RS spectra of representative $CoFe_2O_4$ NPs with different t_m values excited by a laser wavelength of 785 nm, which were normalized to the intensity of the $T_{2g}(2)$ mode at ~475 cm^{-1}.

occupying at lower frequencies, E_g and $T_{2g}(3)$, are attributed to the symmetric and anti-symmetric bending of O atoms in the Fe-/Co–O bonds at the octahedral (BO_6) sites.[41,43,46]

As considering the RS spectra of $CoFe_2O_4$ NPs *versus* various the milling process, the vibration mode at ~566 cm^{-1} ($T_{2g}(1)$) becomes invisible as $t_m = 40$ min. Meanwhile, the other modes still persist, and their peak position tends to shift (about 4–9 cm^{-1}, depending on mode types) towards lower frequencies and their spectral linewidth becomes gradually broadened when t_m increases, particularly the samples with $t_m > 20$ min, see Fig. 6. Basically, the redshift of the modes can be qualitatively explained *via* the expansion of the lattice parameter a *versus* increasing t_m, as shown above. An increase of a reflects an increase of Fe-/Co–O bond distances, which reduces the coupling constant k. Approximately, phonon vibration frequency can be expressed as $f = (1/2\pi)\sqrt{k/m}$, where m is mass of an atom, and the decreased k causes the redshift of the modes. Alternatively, when t_m increases, high pressure and local heating during the milling generate lattice disorders/defects, increasing grain boundaries (due to the reduced d). Broken long-range order of $CoFe_2O_4$ lattice host allows the $q \neq 0$ scattering contributions.[41] Concurrently, some modes with weak intensity (such as $T_{2g}(1)$ in our work) would be extinguished, while the linewidth and peak position of persisting modes broadens and shift, respectively.

It is worth noticing that the intensity ratio between two modes of 617 cm^{-1} ($A_{1g}(2)$ associated with Co at the tetrahedral site) and 475 cm^{-1} ($T_{2g}(2)$, associated with Co at the octahedral site[14]) also varies *versus* t_m, similar to the comparison of the intensity ratio between 617 cm^{-1} ($A_{1g}(2)$) and 686 cm^{-1} ($A_{1g}(1)$) mentioned above. These features reflect the migration of Co and Fe ions between the tetrahedral (A) and octahedral (B) sites as varying t_m. As studying nanostructured cobalt ferrites, it has been suggested that Co^{2+} and Fe^{3+} can occupy both A and B sites (*i.e.*, $0 < \delta < 1$). For spinel-structured materials, however, divalent and trivalent elements usually occupy the A and B sites, respectively.[1,3] The valence identification of Co and Fe in our fabricated cobalt ferrites is thus necessary to clarify the lattice-constant change as well as magnetic behaviors with respect to t_m.

Concerning the valence identification, we have utilized XAS and recorded the Fe and Co K-edge spectra of typical samples, and reference oxides including Fe_2O_3, Fe_3O_4 and CoO. Before measurements, Fe ($E_0 = 7112$ eV) and Co ($E_0 = 7709$ eV) foils were used to calibrate the Fe and Co K-edge energies, respectively. Fig. 7(a) and (b) show the Fe K-edge XAS and first-order derivative spectra of the samples with $t_m = 0$, 60 and 180 min. In the pre-edge region with $E = 7110$–7118 eV, as graphed the inset of Fig. 7(a), a broad hump peaked at ~7114 eV, corresponding to an inflection point in Fig. 7(b), is observed. Basically, the pre-edge peak is associated to the electric quadrupole-forbidden transitions from the O 1s level to 3d transition metals (Fe and Co in the present case). Following the pre-edge region, there is a rapid increase in the XAS intensity of the absorption K-edge. From Fig. 7(b), one can see that the absorption edge of the $CoFe_2O_4$ NPs at ~7122 eV is less independent of t_m, and locates between the absorption edges of Fe_3O_4 (7121 eV) and Fe_2O_3 (~7123 eV). This reflects that both Fe^{2+} and Fe^{3+} ions coexist in our $CoFe_2O_4$ NPs.

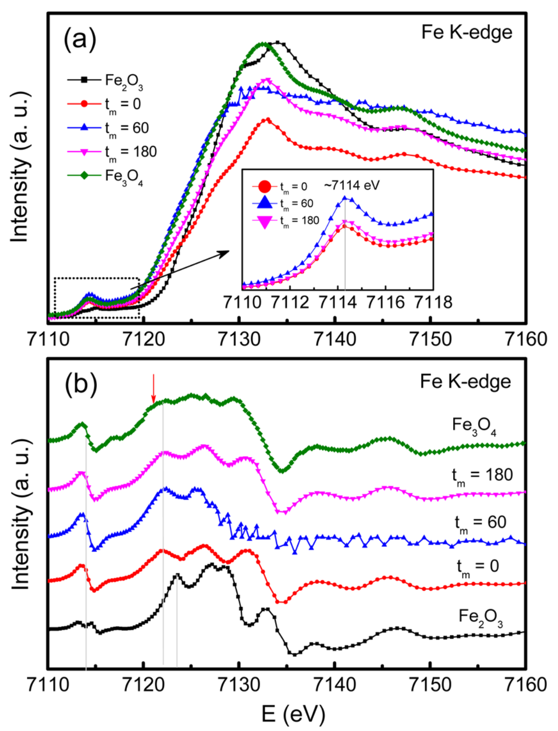

Fig. 7 (a) Fe K-edge XAS data, and (b) their derivative data of typical $CoFe_2O_4$ NPs, $t_m = 0$, 60 and 180 min, compared with those of Fe_2O_3 and Fe_3O_4 references. The inset of (a) plots an enlarged view of the re-edge region.

For the case of Co, its K-edge XAS and first-order derivative spectra of the samples with $t_m = 0$, 10, 60 and 180 min, and CoO are shown in Fig. 8(a)and (b). Evidently, the absorption edges of milled $CoFe_2O_4$ NPs locating at ~7717 eV are almost unchanged *versus* t_m, and well match the absorption edge of CoO, see Fig. 8(b). These results suggest that only Co^{2+} is present in our samples. Notably, in the pre-edge region, the Co K-edge XAS spectrum of the $t_m = 0$ sample has two weak-intensity humps peaked at ~7709.3 (named P_1) and 7712.8 eV (P_2), see the inset of Fig. 8(a). With increasing t_m, P_1 still persists while P_2 becomes invisible as $t_m > 60$ min. Because these pre-edge humps are associated with the occupancy of Co^{2+} in the octahedral and tetrahedral crystal fields,[47] the intensity change of P_1 and P_2 proves the redistribution of Co^{2+} ions in these fields, and milling-induced lattice distortions. Normally, the pre-edge peak due to the octahedral site is broad and more diffused than that due to the tetrahedral site,[37] it is reasonable to assign that P_1 and P_2 are associated with Co^{2+} at the A and B sites, respectively. The intensity decrease of P_2 with increasing t_m indicates the migration of Co^{2+} from the B site to the A site. Additionally, if comparing the pre-edge peaks in the Fe and Co K-edge XAS spectra of all the samples, it comes to our attention that the pre-edge peak at the Fe K-edge is stronger than that at the Co K-edge. It means that at the A site the fraction of $Fe^{2+,3+}$ ions is larger than that of Co^{2+} ions.[48] In other words, the XAS analyses have demonstrated the mixed valence state of $Fe^{2+,3+}$ and Co^{2+} ions in all $CoFe_2O_4$ NPs, and they are present in both the A and B sites, resulting in the mixed spinel type of $(Co_{\delta}{}^{2+}Fe_{1-\delta}{}^{2+,3+})[Co_{1-\delta}{}^{2+}Fe_{1+\delta}{}^{2+,3+}]O_4{}^{2-}$. We think that the migration and redistribution of these ions at the A and B sites together with milling-induced lattice disorders and defects would strongly influence the magnetic behaviors of milled $CoFe_2O_4$ NPs. As studying cobalt ferrites, Singh *et al.*[37] found a coexistence of $Fe^{2+,3+}$ and $Co^{2+,3+}$ ions, but Londo *et al.*[49] found $Co^{2+,3+}$ and Fe^{3+} ions. Meanwhile, some works only found Co^{2+} and Fe^{3+} ions in cobalt ferrites.[41,43,46] Reviewing the previous works on mechanically-milled $CoFe_2O_4$ NPs,[13,16,32,33] one can see that the analyses of electronic structure based on sensitive tools such as X-ray photoelectron spectroscopy (XPS) and XAS were less carried out. Cedeño-Mattei *et al.*[31] studied Mössbauer spectra and suggested the presence of Co^{2+} and Fe^{3+} ions only. Such contradictory results are generated due to the differences in sample fabrication methods and processing conditions, which influence the magnetic properties of cobalt ferrites.

To study the magnetic behaviors, we have measured the field-dependent magnetization, $M(H)$. The $M(H)$ data of representative samples graphed in Fig. 9 reveal all of them exhibiting the hysteresis character. Hysteresis loops have been recorded in the field range $|H| = 0$–7.5 kOe. Their shape is almost unchanged *versus* t_m, excepting the characteristic parameters such as M_s, M_r, and H_c. For M_r and H_c, their values were directly obtained from the intersection points between a $M(H)$ curve and the vertical (M) and horizontal (H) axes, respectively, as illustrated in Fig. 9. Determination of M_s can be based on the law of approach to saturation (LAS), in which H-dependent M obeys the following expression:[50]

$$M = M_s\left(1 - \frac{a'}{H} - \frac{b}{H^2}\right) + \chi H, \tag{1}$$

where a' and χH associated with the inhomogeneities and spontaneous magnetization of domains, respectively, are ignorable as considering a homogeneous ferromagnet at low temperatures and high fields. In other words, eqn (1) can be rewritten as:

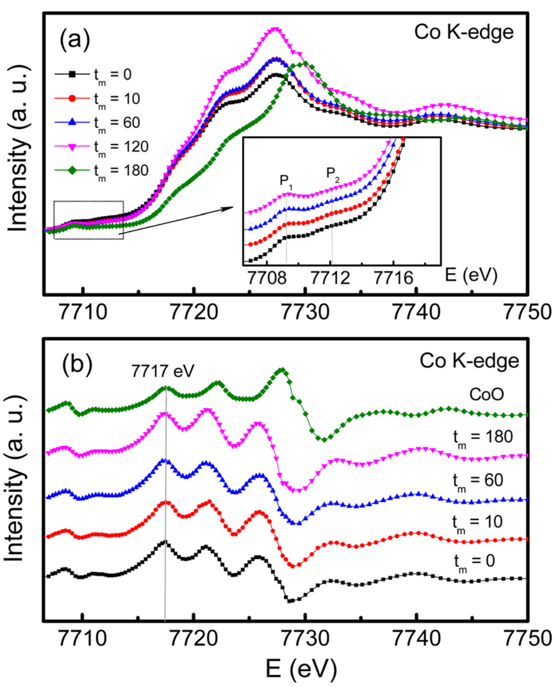

Fig. 8 (a) Co K-edge XAS data, and (b) their derivative data of $CoFe_2O_4$ NPs with $t_m = 0$, 10, 60 and 180 min compared with those of CoO. The inset of (a) is an enlarged view of the pre-edge region.

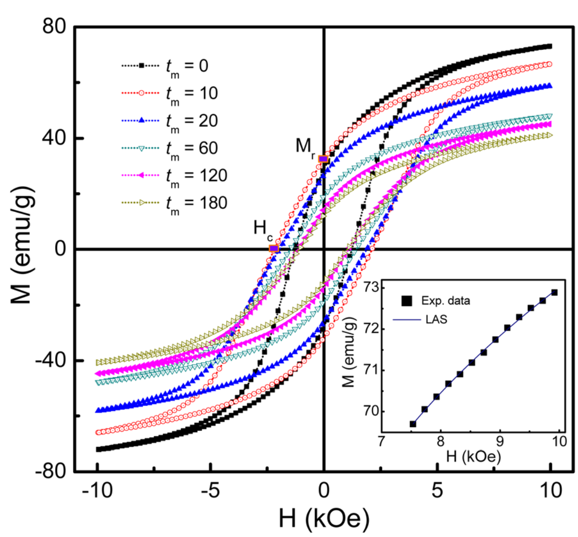

Fig. 9 $M(H)$ hysteresis loops of some representative samples of mechanically-milled $CoFe_2O_4$ NPs. Inset: $M(H)$ data of the as-prepared sample ($t_m = 0$) at fields $H > 7.5$ kOe fitted to the LAS model.

$$M = M_s\left(1 - \frac{b}{H^2}\right), \quad (2)$$

where b is a parameter associated with the magneto-crystalline anisotropy. Fitting $M(H)$ data at fields $H > 7.5$ kOe to eqn (2), as shown representatively in the inset of Fig. 9, we would determine the values of M_s and b, see Table 1 and Fig. 10(a). As shown in Fig. 10(a), M_s gradually decreases from 68.8 emu g^{-1} for the as-prepared sample ($t_m = 0$) to ~34.9 emu g^{-1} for $t_m = 180$ min. A decreasing tendency of M_s as increasing t_m was also observed by Liu and Pedrosa *et al.*[13,16] as investigating mechanically-milled $CoFe_2O_4$ NPs. This phenomenon is mainly explained due to lattice disorders/dislocations formed inside NPs,[13,32] and surface defects acting as a magnetic dead layer.[33] Their density increases with increasing t_m because of the high-energy milling and an increased surface-to-volume ratio. Magnetic moments (or spins) of $Fe^{2+,3+}$ and Co^{2+} ions in these regions become fluctuated, causing short-range magnetic order, that reduce the net magnetic moment or magnetization of milled $CoFe_2O_4$ NPs. Besides these reasons, the migration of Co^{2+} ions from the B site to the A site could also reduce M_s, depending on its concentration, as well as $Fe^{2+,3+}$ concentrations at these sites. Due to equipment limits, we could not estimate their concentrations at the A and B sites (*i.e.*, the degree of inversion δ) in the samples as changing t_m.

Notably, since the crystallite size d gradually decreases as increasing t_m, t_m-dependent interparticle interactions can also influence M_s. It can be could be assessed interparticle interactions based on the M_r/M_s ratio.[51] M_r determined from Fig. 9 reveals its maximum value being about ~34 emu g^{-1} as t_m = 4–8 min, and below and above these t_m values, M_r decreases, see in the inset of Fig. 10(a). From the M_r data, we calculated t_m-dependent M_r/M_s values. As shown in Fig. 10(b), the variation tendency of M_r/M_s is similar to that of M_r. As milling with t_m = 1–10 min, $M_r/M_s > 0.5$ reflects the exchange coupling between neighboring grains/NPs.[52] Beyond these t_m values, the magnetostatic interaction between grains plays a dominant role because $M_r/M_s < 0.5$. Surprisingly, the as-prepared sample (t_m = 0) also belongs to the magnetostatic interaction ($M_r/M_s < 0.5$). This could be due to the magnetostatic interaction additionally dependent on other factors, such as the surface state, isotropy, and aggregation of NPs, apart from the grain size, since SEM images of the samples shown in Fig. 1(a)–(f) have different features. It is necessary to say that $M_r/M_s = 0.5$ corresponds to randomly oriented non-interacting grains (like single domains).[51,53]

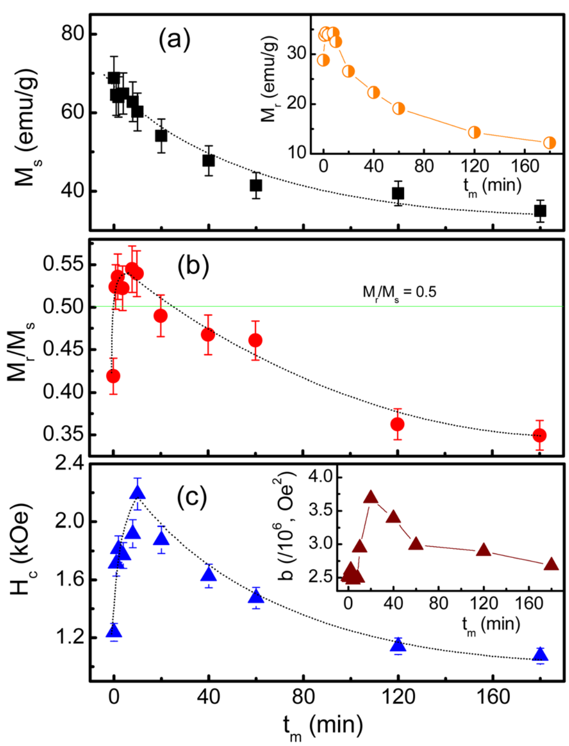

Fig. 10 Variations of (a) M_s, (b) M_r/M_s and (c) H_c as a function of t_m. The insets in (a) and (c) plot t_m-dependent M_r and b data, respectively. Dotted lines are to guide the eyes only.

Such changes in the exchange and magnetostatic interactions *versus* t_m would also influence H_c. This can be clearly seen in Fig. 10(c), where variation tendencies of H_c and M_r/M_s are almost the same. For the $t_m = 0$ sample, H_c is about 1.24 kOe. It rapidly increases to ~2.19 kOe as t_m = 10 min ($d \approx 29$ nm), corresponding to the dominancy of exchange interactions between grains/NPs. As milling with t_m longer than 10 min, the transformation of exchange–magnetostatic interactions reduces gradually H_c to ~1.07 kOe (for t_m = 180 min).

These changes of H_c (as well as M_r and M_r/M_s) are in good agreement with those of the lattice constant a and the ratio $I_{(220)}/I_{(222)}$ with respect to t_m, see Fig. 5(a) and (b) and their inset. It means that H_c of milled $CoFe_2O_4$ NPs is also associated with the distribution of Co^{2+} in the A and B site. As comparing with previous works on mechanically-milled $CoFe_2O_4$ NPs, we have found that the variations of $H_c(t_m)$ in the current work are in good accordance to those reported by Liu and co-workers.[13] However, the differences in $H_c(t_m)$ values reported in literature[13,32,33] are mainly due to initial powders, which may have different sizes, particle morphology, and concentrations of Fe and Co ions at the A and B sites (in which Fe and Co can have oxidation numbers 2+ and 3+, even 4+). These factors are sensitive to sample synthesis methods and processing conditions. In fact, H_c is dependent on not only microstructures, lattice strain/defects,[13,32,54] Co^{2+} distribution and interparticle interactions,[51] but also magnetocrystalline anisotropy characterized by the parameter b. An analogous variation between b and H_c shown in Fig. 10(c) and the inset of Fig. 10(c) proves this statement. It has also been suggested b having the correlation with the anisotropy field (H_a) and anisotropy constant (K_1) as follows:

$$b = \frac{{H_a}^2}{15} = \frac{4{K_1}^2}{15{M_s}^2}. \quad (3)$$

With the obtained b and M_s data, we could calculate H_a and K_1 as using eqn (3). The results shown in Table 1 indicate the variation tendency of H_a similar to that of H_c and b, meaning that H_a reaches to the maximum value at t_m = 10 min ($d \approx 29$

nm). Meanwhile, because K_1 is a function of b and M_s, we have found that a less change of K_1 as t_m = 0–20 min becomes gradually decreased as t_m > 20 min, which is fairly the same as the variation tendency of M_s. Evidently, the data of the magnetic parameters reveal an anomalous variation around the milling time t_m = 10 min ($d \approx 29$ nm), where there is the transformation of exchange-to-magnetostatic interactions, and more Co^{2+} migrates to the A site. As t_m > 10 min, an increase of the surface-to-volume ratio and surface defects enhances the magnetic dead layer, and causes short-range magnetic order, leading to the reduction of the magnetic parameters. With the above results, it is necessary to systematically study other nanostructured cobalt ferrites with different sizes using both XPS and XAS (or Mössbauer) techniques in order to identify the oxidation state and concentration of Fe and Co occupying the A and B sites. Based on these data, one can figure out the origin of the hard-magnetic properties of cobalt ferrites.

4 Conclusion

We based on a coprecipitation method to prepare $CoFe_2O_4$ NPs with $d \approx 81$ nm. These powders were then mechanically milled in air for t_m = 1–180 min to decrease d down to ∼12 nm. Both X-ray and RS studies indicated all the fabricated samples having the cubic-spinel structure. XAS analyses proved the coexistence of $Fe^{2+,3+}$ and Co^{2+} ions in the samples. They occupy both the A and B sites, resulting in the formation of $(Co_{\delta}{}^{2+}Fe_{1-\delta}{}^{2+,3+})[Co_{1-\delta}{}^{2+}Fe_{1+\delta}{}^{2+,3+}]O_4{}^{2-}$ mixed spinel compounds. The features of some characteristic XRD peaks and Raman modes, and the pre-edge XAS spectra revealed the migration and redistribution of the cations between the A and B sites, which would influence the lattice constant a of milled $CoFe_2O_4$ NPs. Particularly, as changing t_m from 1 to 10 min, we found H_c of $CoFe_2O_4$ NPs shifts towards the hard-magnetic behavior, which is related to the exchange coupling between neighboring grains, due to $M_r/M_s > 0.5$. Meanwhile, the decrease of H_c as t_m > 10 min is related to the magnetostatic interaction between grains, due to $M_r/M_s < 0.5$. For M_s, its gradual decrease with respect to t_m is mainly due to enhancements of surface defects and the thickness of magnetic-dead layers, which cause short-range magnetic order, consequently the reduction of M_s.

Author contributions

D. H. Manh, and T. D. Thanh: Conceptualization, Methodology and Writing; T. L. Phan, and D. S. Yang: Investigation and Reviewing.

Conflicts of interest

The authors declare no competing financial interest.

Acknowledgements

This work was supported by the Excellence Research Team Development Program at the Vietnam Academy of Science and Technology NCXS01.04/22-24.

References

1 T. Tatarchuk, M. Bououdina, J. Judith Vijaya and L. John Kennedy, *Spinel Ferrite Nanoparticles: Synthesis, Crystal Structure, Properties, and Perspective Applications*, 2017, pp. 305–325, DOI: 10.1007/978-3-319-56422-7_22.

2 Y. Oh, M. Sahu, S. Hajra, A. M. Padhan, S. Panda and H. J. Kim, Spinel Ferrites (CoFe2O4): Synthesis, Magnetic Properties, and Electromagnetic Generator for Vibration Energy Harvesting, *J. Electron. Mater.*, 2022, **51**, 1933–1939, DOI: 10.1007/s11664-022-09551-5.

3 V. Tsurkan, H.-A. Krug von Nidda, J. Deisenhofer, P. Lunkenheimer and A. Loidl, On the complexity of spinels: Magnetic, electronic, and polar ground states, *Phys. Rep.*, 2021, **926**, 1–86, DOI: 10.1016/j.physrep.2021.04.002.

4 K. Malaie and M. R. Ganjali, Spinel nano-ferrites for aqueous supercapacitors; linking abundant resources and low-cost processes for sustainable energy storage, *J. Energy Storage*, 2021, **33**, 102097, DOI: 10.1016/j.est.2020.102097.

5 (*a*) T. N. Pham, T. Q. Huy and A. T. Le, Spinel ferrite (AFe_2O_4)-based heterostructured designs for lithium-ion battery, environmental monitoring, and biomedical applications, *RSC Adv.*, 2020, **10**, 31622–31661, DOI: 10.1039/D0RA05133K; (*b*) X. Meng, L. He, Y. Liu, Y. Yu and W. Yang, Carbon-coated defect-rich $MnFe_2O_4$/MnO heterojunction for high-performance microwave absorption, *Cacbon*, 2022, **194**, 207–219, DOI: 10.1016/j.carbon.2022.03.075.

6 R. K. Kotnala and J. Shah, Chapter 4 - Ferrite Materials: Nano to Spintronics Regime, *Handbook of Magnetic Materials*, 2015, vol. 23, pp. 291–379, DOI: 10.1016/B978-0-444-63528-0.00004-8.

7 (*a*) M. Matsuda, H. Ueda, A. Kikkawa, Y. Tanaka, K. Katsumata, Y. Narumi, T. Inami, Y. Ueda and S. H. Lee, Spin–lattice instability to a fractional magnetization state in the spinel $HgCr_2O_4$, *Nat. Phys.*, 2007, **3**, 397–400, DOI: 10.1038/nphys586; (*b*) M. A. Ali, M. M. Uddin, M. N. I. Khan, F. U. Z. Chowdhury and S. M. Haque, Structural, morphological and electrical properties of Sn-substituted Ni-Zn ferrites synthesized by double sintering technique, *J. Magn. Magn. Mater.*, 2017, **424**, 148–154, DOI: 10.1016/j.jmmm.2016.10.027.

8 K. R. Sanchez-Lievanos, J. L. Stair and K. E. Knowles, Cation Distribution in Spinel Ferrite Nanocrystals: Characterization, Impact on their Physical Properties, and Opportunities for Synthetic Control, *Inorg. Chem.*, 2021, **60**, 4291–4305, DOI: 10.1021/acs.inorgchem.1c00040.

9 F. Xu, X. Li, G. Gan, S. Fan, Z. Yin, L. Wang, M. Qin, M. O. Tadé and S. Liu, Manganese-Based Spinel Core–Shell Nanostructures for Efficient Electrocatalysis of 1,2-Dichloroethane, *ACS Appl. Nano Mater.*, 2020, **3**, 10778–10786, DOI: 10.1021/acsanm.0c02099.

10 N. Garg, Menaka, K. V. Ramanujachary, S. E. Lofland and A. K. Ganguli, Nanostructured dimagnesium manganese oxide (Spinel): Control of size, shape and their magnetic

and electro catalytic properties, *J. Solid State Chem.*, 2013, **197**, 392–397, DOI: 10.1016/j.jssc.2012.08.063.

11 S. C. Goh, C. H. Chia, S. Zakaria, M. Yusoff, C. Y. Haw, S. Ahmadi, N. M. Huang and H. N. Lim, Hydrothermal preparation of high saturation magnetization and coercivity cobalt ferrite nanocrystals without subsequent calcination, *Mater. Chem. Phys.*, 2010, **120**, 31–35, DOI: 10.1016/j.matchemphys.2009.10.016.

12 C. Zhao, A. Gao, Y. Yang, C. Tu, A. Bhutani, K. A. Walsh, S. Gong and D. P. Shoemaker, High-quality $CoFe_2O_4$ thin films with large coercivity grown via a wet chemical route, *AIP Adv.*, 2019, **9**, 035126, DOI: 10.1063/1.5085232.

13 B. H. Liu, J. Ding, Z. L. Dong, C. B. Boothroyd, J. H. Yin and J. B. Yi, Microstructural evolution and its influence on the magnetic properties of CoFe2O4 powders during mechanical milling, *Phys. Rev. B: Condens. Matter Mater. Phys.*, 2006, **74**, 184427, DOI: 10.1103/PhysRevB.74.184427.

14 S. Singh and N. Khare, Low field magneto-tunable photocurrent in $CoFe_2O_4$ nanostructure films for enhanced photoelectrochemical properties, *Sci. Rep.*, 2018, **8**, 6522, DOI: 10.1038/s41598-018-24947-2.

15 N. Hosni, K. Zehani, T. Bartoli, L. Bessais and H. Maghraoui-Meherzi, Semi-hard magnetic properties of nanoparticles of cobalt ferrite synthesized by the co-precipitation process, *J. Alloys Compd.*, 2017, **694**, 1295–1301, DOI: 10.1016/j.jallcom.2016.09.252.

16 F. J. Pedrosa, J. Rial, K. M. Golasinski, M. N. Guzik, A. Quesada, J. F. Fernández, S. Deledda, J. Camarero and A. Bollero, Towards high performance $CoFe_2O_4$ isotropic nanocrystalline powder for permanent magnet applications, *Appl. Phys. Lett.*, 2016, **109**, 223105, DOI: 10.1063/1.4969064.

17 P. Maltoni, T. Sarkar, G. Barucca, G. Varvaro, F. Locardi, D. Peddis and R. Mathieu, Tuning the Magnetic Properties of Hard–Soft $SrFe_{12}O_{19}/CoFe_2O_4$ Nanostructures via Composition/Interphase Coupling, *J. Phys. Chem. C*, 2021, **125**, 5927–5936, DOI: 10.1021/acs.jpcc.1c00355.

18 (*a*) Z. Ž. Lazarević, Č. Jovalekić, A. Milutinović, D. Sekulić, V. N. Ivanovski, A. Rečnik, B. Cekić and N. Ž. Romčević, Nanodimensional spinel $NiFe_2O_4$ and $ZnFe_2O_4$ ferrites prepared by soft mechanochemical synthesis, *J. Appl. Phys.*, 2013, **113**, 187221, DOI: 10.1063/1.4801962; (*b*) S. Iraqui, S. S. Kashyap and M. H. Rashid, NiFe2O4 nanoparticles: an efficient and reusable catalyst for the selective oxidation of benzyl alcohol to benzaldehyde under mild conditions, *Nanoscale Adv.*, 2020, **2**, 5790–5802, DOI: 10.1039/D0NA00591F; (*c*) C. Yao, Q. Zeng, G. F. Goya, T. Torres, J. Liu, H. Wu, M. Ge, Y. Zeng, Y. Wang and J. Z. Jiang, ZnFe2O4 Nanocrystals: Synthesis and Magnetic Properties, *J. Phys. Chem. C*, 2007, **111**, 12274–12278, DOI: 10.1021/jp0732763; (*d*) M. A. Ali, M. N. I. Khan, F. Chowdhury, *et al.*, Yttrium-substituted Mg–Zn ferrites: correlation of physical properties with Yttrium content, *J. Mater. Sci.: Mater. Electron.*, 2019, **30**, 13258–13270, DOI: 10.1007/s10854-019-01689-z.

19 J. L. Ortiz-Quiñonez, U. Pal and M. S. Villanueva, Structural, Magnetic, and Catalytic Evaluation of Spinel Co, Ni, and Co–Ni Ferrite Nanoparticles Fabricated by Low-Temperature Solution Combustion Process, *ACS Omega*, 2018, **3**, 14986–15001, DOI: 10.1021/acsomega.8b02229.

20 Y. H. Hou, Y. J. Zhao, Z. W. Liu, H. Y. Yu, X. C. Zhong, W. Q. Qiu, D. C. Zeng and L. S. Wen, Structural, electronic and magnetic properties of partially inverse spinel $CoFe_2O_4$: a first-principles study, *J. Phys. D: Appl. Phys.*, 2010, **43**, 445003, DOI: 10.1088/0022-3727/43/44/445003.

21 S. E. Shirsath, D. Wang, J. Zhang, A. Morisako, S. Li and X. Liu, Single-Crystal-like Textured Growth of $CoFe_2O_4$ Thin Film on an Amorphous Substrate: A Self-Bilayer Approach, *ACS Appl. Electron. Mater.*, 2020, **2**, 3650–3657, DOI: 10.1021/acsaelm.0c00716.

22 S. Moosavi, S. Zakaria, C. H. Chia, S. Gan, N. A. Azahari and H. Kaco, Hydrothermal synthesis, magnetic properties and characterization of $CoFe_2O_4$ nanocrystals, *Ceram. Int.*, 2017, **43**, 7889–7894, DOI: 10.1016/j.ceramint.2017.03.110.

23 A. Hajalilou, S. A. Mazlan, M. Abbasi and H. Lavvafi, Fabrication of spherical $CoFe_2O_4$ nanoparticles *via* sol–gel and hydrothermal methods and investigation of their magnetorheological characteristics, *RSC Adv.*, 2016, **6**, 89510–89522, DOI: 10.1039/C6RA13493A.

24 M. Houshiar, F. Zebhi, Z. J. Razi, A. Alidoust and Z. Askari, Synthesis of cobalt ferrite ($CoFe_2O_4$) nanoparticles using combustion, coprecipitation, and precipitation methods: A comparison study of size, structural, and magnetic properties, *J. Magn. Magn. Mater.*, 2014, **371**, 43–48, DOI: 10.1016/j.jmmm.2014.06.059.

25 Z. Zi, Y. Sun, X. Zhu, Z. Yang, J. Dai and W. Song, Synthesis and magnetic properties of $CoFe_2O_4$ ferrite nanoparticles, *J. Magn. Magn. Mater.*, 2009, **321**, 1251–1255, DOI: 10.1016/j.jmmm.2008.11.004.

26 H. Latiff, M. Kishimoto, J. Inoue, E. Kita, H. Yanagihara and T. Devillers, Coercivity analysis of cubic and tetragonal (Cu,Co) ferrite particles within the global model, *J. Magn. Magn. Mater.*, 2019, **489**, 165380, DOI: 10.1088/1361-6463/abe5e1.

27 E. Lima, E. L. Winkler, D. Tobia, H. E. Troiani, R. D. Zysler, E. Agostinelli and D. Fiorani, Bimagnetic CoO Core/$CoFe_2O_4$ Shell Nanoparticles: Synthesis and Magnetic Properties, *Chem. Mater.*, 2012, **24**, 512–516, DOI: 10.1021/cm2028959.

28 L. Pan, D. Cao, P. Jing, J. Wang and Q. Liu, A novel method to fabricate $CoFe_2O_4/SrFe_{12}O_{19}$ composite ferrite nanofibers with enhanced exchange coupling effect, *Nanoscale Res. Lett.*, 2015, **10**, 131, DOI: 10.1186/s11671-015-0829-z.

29 Z. Wang, X. Liu, M. Lv, P. Chai, Y. Liu, X. Zhou and J. Meng, Preparation of One-Dimensional $CoFe_2O_4$ Nanostructures and Their Magnetic Properties, *J. Phys. Chem. C*, 2008, **112**, 15171–15175, DOI: 10.1021/jp802614v.

30 Y. C. Wang, J. Ding, J. B. Yi, B. H. Liu, T. Yu and Z. X. Shen, High-coercivity Co-ferrite thin films on (100)-SiO2(100)-SiO2 substrate, *Appl. Phys. Lett.*, 2004, **84**, 2596–2598, DOI: 10.1063/1.1695438.

31 Y. Cedeño-Mattei, O. Perales-Pérez and O. N. C. Uwakweh, Show more Effect of high-energy ball milling time on structural and magnetic properties of nanocrystalline

cobalt ferrite powders, *J. Magn. Magn. Mater.*, 2013, **341**, 17–24, DOI: 10.1016/j.jmmm.2013.04.015.
32 A. S. Ponce, E. F. Chagas, R. J. Prado, C. H. M. Fernandes, A. J. Terezo and E. Baggio-Saitovitch, High coercivity induced by mechanical milling in cobalt ferrite powder, *J. Magn. Magn. Mater.*, 2013, **344**, 182–187, DOI: 10.1016/j.jmmm.2013.05.056.
33 F. J. Pedrosa, J. Rial, K. M. Golasinski, M. Rodríguez-Osorio, G. Salas, D. Granados, J. Camarero and A. Bollero, Tunable nanocrystalline $CoFe_2O_4$ isotropic powders obtained by co-precipitation and ultrafast ball milling for permanent magnet applications, *RSC Adv.*, 2016, **6**, 87282–87287, DOI: 10.1039/C6RA15698C.
34 B. J. Rani, M. Ravina, B. Saravanakumar, G. Ravi, V. Ganesh, S. Ravichandran and R. Yuvakkumar, Ferrimagnetism in cobalt ferrite (CoFe2O4) nanoparticles, *Nano-Struct. Nano-Objects*, 2018, **14**, 84–91, DOI: 10.1016/j.nanoso.2018.01.012.
35 S. Li, T. Zhang, R. Tang, H. Qiu, C. Wang and Z. Zhou, Solvothermal synthesis and characterization of monodisperse superparamagnetic iron oxide nanoparticles, *J. Magn. Magn. Mater.*, 2015, **379**, 226–231, DOI: 10.1016/j.jmmm.2014.12.054.
36 S. C. Endres, L. C. Ciacchi and L. Mädler, A review of contact force models between nanoparticles in agglomerates, aggregates, and films, *J. Aerosol Sci.*, 2021, **153**, 105719, DOI: 10.1016/j.jaerosci.2020.105719.
37 M. N. Singh, A. K. Sinha and H. Ghosh, Determination of transition metal ion distribution in cubic spinel $Co_{1.5}Fe_{1.5}O_4$ using anomalous x-ray diffraction, *AIP Adv.*, 2015, **5**, 087115, DOI: 10.1063/1.4928425.
38 G. K. Williamson and W. H. Hall, X-ray line broadening from filed aluminium and wolfram, *Acta Metall.*, 1953, **1**, 22–31, DOI: 10.1016/0001-6160(53)90006-6.
39 S. Tsunekawa, K. Ishikawa, Z.-Q. Li, Y. Kawazoe and A. Kasuya, Origin of Anomalous Lattice Expansion in Oxide Nanoparticles, *Phys. Rev. Lett.*, 2000, **85**, 3440–3443, DOI: 10.1103/PhysRevLett.89.249905.
40 V. Šepelák, D. Baabe, D. Mienert, D. Schultze, F. Krumeich, F. J. Litterst, K. D. Becker, V. Šepelák, D. Baabe, D. Mienert, D. Schultze, F. Krumeich, F. J. Litterst and K. D. Becker, *J. Magn. Magn. Mater.*, 2003, **257**, 377–386, DOI: 10.1016/S0304-8853(02)01279-9.
41 P. Chandramohan, M. P. Srinivasan, S. Velmurugan, S. V. Narasimhan, P. Chandramohan, M. P. Srinivasan, S. Velmurugan and S. V. Narasimhan, *J. Solid State Chem.*, 2011, **184**, 89–96, DOI: 10.1016/j.jssc.2010.10.019.
42 *Pressure-Induced Phase Transitions in AB2X4 Chalcogenide Compounds*, ed. F. J. Manjon, I. Tiginyanu and V. Ursaki, Springer Berlin Heidelberg, Berlin, Heidelberg, 2014, vol. 189.
43 S. M. Ansari, B. B. Sinha, D. Phase, D. Sen, P. U. Sastry, Y. D. Kolekar and C. V. Ramana, Particle Size, Morphology, and Chemical Composition Controlled $CoFe_2O_4$ Nanoparticles with Tunable Magnetic Properties via Oleic Acid Based Solvothermal Synthesis for Application in Electronic Devices, *ACS Appl. Nano Mater.*, 2019, **2**, 1828–1843, DOI: 10.1021/acsanm.8b02009.
44 D. M. Phase, S. Tiwari, R. Prakash, A. Dubey, V. G. Sathe, R. J. Choudhary, D. M. Phase, S. Tiwari, R. Prakash, A. Dubey, V. G. Sathe and R. J. Choudhary, *J. Appl. Phys.*, 2006, **100**, 123703, DOI: 10.1063/1.2403849.
45 M. Baghaie Yazdi, K.-Y. Choi, D. Wulferding, P. Lemmens and L. Alff, Raman study of the Verwey transition in magnetite thin films, *New J. Phys.*, 2013, **15**, 103032, DOI: 10.1088/1367-2630/15/10/103032.
46 S. M. Ansari, K. C. Ghosh, R. S. Devan, D. Sen, P. U. Sastry, Y. D. Kolekar and C. V. Ramana, Eco-Friendly Synthesis, Crystal Chemistry, and Magnetic Properties of Manganese-Substituted $CoFe_2O_4$ Nanoparticles, *ACS Omega*, 2020, **5**, 19315–19330, DOI: 10.1021/acsomega.9b02492.
47 S. Ammar, A. Helfen, N. Jouini, F. Fiévet, I. Rosenman, F. Villain, P. Molinié and M. Danot, Magnetic properties of ultrafine cobalt ferrite particles synthesized by hydrolysis in a polyol medium, *J. Mater. Chem.*, 2001, **11**, 186–192, DOI: 10.1039/b003193n.
48 D. Carta, A. Corrias, A. Falqui, R. Brescia, E. Fantechi, F. Pineider and C. Sangregorio, EDS, HRTEM/STEM, and X-ray absorption spectroscopy studies of co-substituted maghemite nanoparticles, *J. Phys. Chem. C*, 2013, **117**, 9496–9506, DOI: 10.1021/jp401706c.
49 S. Londo, S. Biswas, J. Husek, I. V. Pinchuk, M. J. Newburger, A. Boyadzhiev, A. H. Trout, D. W. McComb, R. Kawakami and L. R. Baker, Ultrafast Spin Crossover in a Room-Temperature Ferrimagnet: Element-Specific Spin Dynamics in Photoexcited Cobalt Ferrite, *J. Phys. Chem. C*, 2020, **124**, 11368–11375, DOI: 10.1021/acs.jpcc.0c03736.
50 J. Lee, E. J. Lee, T.-Y. Hwang, J. Kim and Y.-H. Choa, Anisotropic characteristics and improved magnetic performance of Ca–La–Co-substituted strontium hexaferrite nanomagnets, *Sci. Rep.*, 2020, **10**, 15929, DOI: 10.1038/s41598-020-72608-0.
51 S. H. C. Sushin Chikazumi, *Physics of Magnetism*, Krieger Pub Co, 1978.
52 J. N. Dahal, D. Neupane and S. R. Mishra, Exchange-Coupling Behavior in $SrFe_{12}O_{19}/La_{0.7}Sr_{0.3}MnO_3$ Nanocomposites, *Ceramics*, 2019, **2**, 100–111, DOI: 10.3390/ceramics2010010.
53 E. C. Stone and E. P. Wohlfarth, A mechanism of magnetic hysteresis in heterogeneous alloys, *Philos. Trans. R. Soc. London, Ser. A*, 1948, **240**, 599–642, DOI: 10.1098/rsta.1948.0007.
54 S. Singh, S. Munjal and N. Khare, Strain/defect induced enhanced coercivity in single domain $CoFe_2O_4$ nanoparticles, *J. Magn. Magn. Mater.*, 2015, **386**, 69–73, DOI: 10.1016/j.jmmm.2015.03.057.